Redox Biology 80 (2025) 103528

Contents lists available at ScienceDirect

Redox Biology

journal homepage: www.elsevier.com/locate/redox

Niraparib restricts intraperitoneal metastases of ovarian cancer by eliciting CD36-dependent ferroptosis

Ning Jin [a,b,1], Yi-yu Qian [a,b,1], Xiao-fei Jiao [a,b,1], Zhen Wang [c,d], Xin Li [a,b], Wen Pan [a,b], Jin-kai Jiang [a,b], Pu Huang [e], Si-yuan Wang [f], Ping Jin [a,b], Qing-lei Gao [a,b,**], Dan Liu [a,b,***], Yu Xia [a,b,*]

[a] Cancer Biology Research Center (Key Laboratory of Chinese Ministry of Education), Tongji Hospital Tongji Medical College Huazhong University of Science and Technology, 1095 Jiefang Ave, Wuhan, 430030, China
[b] Department of Gynecology and Obstetrics, Tongji Hospital Tongji Medical College Huazhong University of Science and Technology, Wuhan, 430030, China
[c] Department of Obstetrics, Zhongnan Hospital of Wuhan University, Wuhan, Hubei, China
[d] Clinical Medicine Research Centre of Prenatal Diagnosis and Birth Health in Hubei Province, Wuhan, Hubei, China
[e] Department of Obstetrics and Gynecology, Shandong Provincial Hospital Affiliated to Shandong First Medical University, Jinan, China
[f] Department of Geriatrics, Tongji Hospital, Tongji Medical College, Huazhong University of Science and Technology, Wuhan, 430030, China

ARTICLE INFO

Keywords:
Ovarian cancer
Niraparib
Intraperitoneal metastases
Ferroptosis
Fatty acid
CD36

ABSTRACT

Ovarian cancer (OC) is prone to peritoneum or omentum dissemination, thus giving rise to the formidable challenge of unresectable surgery and a dismal survival rate. Although niraparib holds a pivotal role in the maintenance treatment of OC, its effect on suppressing metastases during primary intervention remains enigmatic. Recently, we initiated a prospective clinical study (NCT04507841) in order to evaluate the therapeutic efficacy of neoadjuvant niraparib monotherapy for advanced OC with homologous recombination deficiency. An analysis of patient tumor burden before and after the niraparib challenge showed a remarkable vulnerability of OC intraperitoneal metastases to niraparib exposure. This killing capacity of niraparib was closely associated with the accumulation of fatty acids within the abdomen, which was confirmed by the increased susceptibility of tumor cells to niraparib treatment in the presence of fatty acids. In the context of abundant fatty acids, niraparib elevated intracellular levels of fatty acids and lipid peroxidation, leading to subsequent tumor cell ferroptosis in a p53 and BRCA-independent manner. Notably, under niraparib exposure, a critical fatty acid transporter CD36 was dramatically upregulated in tumors, facilitating excessive uptake of fatty acids. Pharmacological inhibition of either ferroptosis or CD36 impaired the anti-tumor activity of niraparib both *in vitro* and in murine intraperitoneal ID8 tumor models. Our findings demonstrate ferroptosis as a novel mechanism underlying the regression of OC metastases induced by niraparib, thereby offering tantalizing prospects for the frontline application of this agent in the management of OC.

1. Introduction

Ovarian cancer (OC) exhibits a high mortality rate and has emerged as the fifth leading cause of cancer-related deaths among gynecologic malignancies with a slight enhancement in survival rates over recent decades [1,2]. OC frequently originates in the distal fimbriae of the fallopian tube and tends to metastasize to the peritoneal cavity, the lipid-rich omentum, and adjacent organs [3,4]. Consequently, optimal cytoreductive surgery is hard to achieve in patients with extensive miliary intraperitoneal lesions [5,6]. In this context, neoadjuvant

* Corresponding author. Cancer Biology Research Center (Key Laboratory of Chinese Ministry of Education), Tongji Hospital Tongji Medical College Huazhong University of Science and Technology, 1095 Jiefang Ave, Wuhan, 430030, China.Xiayu_hb@tjh.tjmu.edu.cn
** Corresponding author. Cancer Biology Research Center (Key Laboratory of Chinese Ministry of Education), Tongji Hospital Tongji Medical College Huazhong University of Science and Technology, 1095 Jiefang Ave, Wuhan, 430030, China.
*** Corresponding author. Cancer Biology Research Center (Key Laboratory of Chinese Ministry of Education), Tongji Hospital Tongji Medical College Huazhong University of Science and Technology, 1095 Jiefang Ave, Wuhan, 430030, China.
E-mail addresses: qlgao@tjh.tjmu.edu.cn (Q.-l. Gao), tj_liudan@tjh.tjmu.edu.cn (D. Liu).
[1] Contributed equally.

https://doi.org/10.1016/j.redox.2025.103528
Received 22 January 2025; Accepted 1 February 2025
Available online 3 February 2025

chemotherapy (NACT) has garnered extensive clinical application, offering the potential of debulking surgery and enhancing the prospects of achieving complete resection [5,7]. However, this approach increases the risk of inducing resistance to subsequent platinum-based chemotherapy in the residual cancer cells, driven by the enhancement of stem-like properties and gene mutations, culminating in the development of multi-drug resistance in OC patients [8]. Therefore, the identification of a feasible solution for regression or elimination of OC metastatic foci is urgently needed, which may improve the prognosis of patients with advanced OC.

As the most common subtype, high-grade serous ovarian cancer (HGSOC) accounts for nearly 80 % of all OC deaths [9]. The hallmark characteristics of HGSOC encompass genetic alterations, such as the inactivation or truncation of the tumor protein p53 (*TP53*) gene in up to 96 % of all cases and the mutation of *BRCA1/2* in approximately 16%–23 % of cases [10,11]. Specifically, *BRCA1/2* mutation results in genomic homologous recombination deficiency (HRD), rendering tumors more susceptible to poly (ADP-ribose) polymerase inhibitors (PARPis) due to the established action of synthetic lethality and pioneering a new era of precision medicine [12]. One of the PARPis, niraparib, has been demonstrated to improve progression-free survival (PFS) of OC patients in the late-line setting by the QUADRA study [13] and maintenance therapy in NOVA, NORA, PRIMA, and PRIME clinical trials [14–17]. Nowadays, niraparib has been approved by the Food and Drug Administration (FDA) in maintenance therapy after platinum-based chemotherapy or as a therapeutic option for recurrent disease [18,19]. Nonetheless, the feasibility of employing niraparib in the neoadjuvant therapy to mitigate platinum-based chemoresistance and maximize the benefits of debulking surgery for patients with unresectable lesions warrants further exploration.

Based on a prospective clinical trial, we collected tumor samples and prognosis data from enrolled patients with pre- and post-niraparib monotherapy. We observed that niraparib exerts a profound inhibitory effect on OC metastatic lesions. This preferential suppression of metastatic lesions was due to the excessive fatty acid accumulation in tumor beds and subsequent induction of ferroptosis following the niraparib challenge. Interference of ferroptosis or fatty acid uptake delayed niraparib-induced metastase rejection in both immunodeficient and immunocompetent syngeneic models. Thus, we have elucidated a novel mechanism underpinning the regression of OC metastasis by niraparib, providing a preclinical proof of concept for niraparib as a neoadjuvant strategy for the treatment of OC.

2. Materials and methods

2.1. Sample collection

The pre-treated tumor samples were obtained from biopsies of patients enrolled in the NANT clinical trial (NCT04507841). The post-treated tumor samples were collected at surgery from patients who had received 2 cycles of niraparib administration. This clinical trial is the first prospective, single-armed, phase II prospective study to evaluate the efficacy and safety of niraparib as neoadjuvant therapy for newly diagnosed HGSOC with HRD. In this trial, patients would receive neoadjuvant treatment followed by interval debulking surgery, allowing us to fully understand the relationship between the HR status and the efficacy of neoadjuvant therapy [20].

We collected 5 paired metastatic tumor lesions from 5 patients to perform bulk RNA sequencing (bulk RNA-seq, the baseline information of these patients was listed in Table 1), 13 paired computed tomography (CT) images from 13 patients to figure out the effect of niraparib on different lesions (The baseline information of these patients was listed in Table 2), 10 paired tumor samples from 10 patients for immunohistochemistry (IHC) analysis, Hematoxylin and Eosin (H&E) staining, and oil red O staining (The baseline information of these patients was listed in Table 3), 1 fresh tumor from 1 patient for patient-derived xenograft (PDX) generation (The baseline information of the patient was listed in Table 4), 19 niraparib pre-treated and 18 post-treated clinical frozen metastatic tissues for widely targeted metabolomics (The baseline information of these patients was listed in Table 5).

2.2. Animal purchase and raising

Four-week-old female BALB/c nude mice and C57BL/6 mice were purchased from Gempharmatech Co., Ltd and raised in the specific pathogen-free (SPF) laboratory animal center of Tongji Hospital affiliated to Huazhong University of Science and Technology. The ethical approval number is TJH-202204005, and the animal experiment operators have obtained animal qualification certificates and complied with the ethical requirements throughout the operation.

2.3. The PDX model

Fresh tumor tissue samples were collected from consenting patients who had undergone surgical resection of OC. Samples were trimmed and cut into 10 mm^3 pieces. BALB/c nude mice were anesthetized with 2 % isoflurane and tumor pieces were implanted subcutaneously on the dorsum as a first-generation PDX model. The size of the subcutaneous tumor was measured every 2 days. When the diameter reached 20 mm, the tumor tissue was cut into pieces and transplanted into the dorsum of the new BALB/c nude mice as the next-generation PDX model. Seven days after the establishment of the PDX models, mice were randomly assigned to the vehicle group (n = 5), the niraparib (Beigene, 50 mg/kg, intragastrically) single agent group (n = 5), the sulfosuccinimidyl oleate sodium (SSO, MCE, 50 mg/kg, HY-112847A, intragastrically) single agent group (n = 5), and the combined treatment of niraparib with SSO

Table 2
Patient information for CT images.

Patient_ID	Age	Stage	Pathological_type	HRD	GIS	BRCA
01006	49	IIIC	HGSOC	P	22	P
01016	36	IV	HGSOC	P	40	P
01025	49	IIIC	HGSOC	P	70	P
01026	60	IIIC	HGSOC	P	51	P
01045	48	IIIC	HGSOC	P	89	P
01046	50	IIIA	HGSOC	P	69	P
01047	53	IV	HGSOC	P	69	N
01068	68	IIIC	HGSOC	P	53	P
01069	58	IIIC	HGSOC	P	66	N
01071	63		HGSOC	P	62	N
01075	63	IVA	HGSOC	P	50	P
01077	68	IIIC	HGSOC	P	85	N
01078	43		HGSOC	P	62	N

Table 1
Patient information for bulk RNAseq.

Patient_ID	Age	Stage	Pathological_type	HRD	GIS	BRCA	Sample_site
01025	49	IIIC	HGSOC	P	70	P	Metastasis
01030	48	IIIC	HGSOC	P	70	N	Metastasis
02003	68	IV	HGSOC	P	77	N	Metastasis
01041	56	IIIC	HGSOC	P	17	P	Metastasis
01016	36	IV	HGSOC	P	40	P	Metastasis

Table 3
Patient information for H&E, oil red O, and IHC staining.

Patient_ID	Age	Stage	Pathological_type	HRD	GIS	BRCA
01006	49	IIIC	HGSOC	P	22	P
01013	50	IIIC	HGSOC	P	64	P
01007	52	IIIC	HGSOC	P	66	N
02001	60	IV	HGSOC	P	72	N
01036	62	IIIC	HGSOC	P	79	N
01016	36	IV	HGSOC	P	40	P
01020	52	IIIC	HGSOC	N	34	N
01040	67	IV	HGSOC	N	26	N
01062	55		HGSOC	P	55	N
01065	59	IIIC	HGSOC	N	0	N

Table 4
Patient information for PDX.

Patient_ID	Age	Stage	Pathological_type	HRD	GIS	BRCA
01007	52	IIIC	HGSOC	P	66	N

Table 5
Patient information for widely targeted metabolomics.

Patient_ID	Treatment	Site
01062	Pre and Post	Metastasis
01072	Pre and Post	Metastasis
01007	Pre	Metastasis
01009	Pre	Metastasis
01078	Post	Metastasis
01014	Pre	Metastasis
01016	Pre	Metastasis
02001	Pre	Metastasis
01022	Pre and Post	Metastasis
01024	Pre and Post	Metastasis
01025	Pre and Post	Metastasis
01020	Post	Metastasis
01023	Pre	Metastasis
01030	Post	Metastasis
01043	Pre and Post	Metastasis
01044	Post	Metastasis
01091	Post	Metastasis
01097	Pre	Metastasis-1
01097	Pre	Metastasis-2
01096	Pre	Metastasis
01083	Post	Metastasis-1
01083	Post	Metastasis-2
01088	Pre	Metastasis
01087	Pre	Metastasis
02009	Pre	Metastasis
18005	Post	Metastasis
10011	Post	Metastasis
01065	Post	Metastasis
01067	Post	Metastasis
01063	Pre	Metastasis
01078	Post	Metastasis

group (n = 5). Tumor burden was monitored daily, and the tumor volume was calculated according to the equation volume = length × width × width × 1/2. Thereafter, on day 33, all the mice were humanely sacrificed under anesthesia. Macroscopic lesions were recorded, and tumor nodules were dissected, weighted, and paraffin-embedded for subsequent detection.

2.4. The ID8 tumor-bearing BALB/c nude mouse model

5×10^6 ID8 cells were injected intraperitoneally into BALB/c nude mice. After 3 days of injection, mice were randomly assigned to the control group (n = 3), the niraparib (Beigene, 50 mg/kg, intragastrically) single agent group (n = 3), the Lipro-1 (MCE, 10 mg/kg, HY-12726, intraperitoneally) single agent group (n = 3), the combined treatment of niraparib with Lipro-1 group (n = 3). Tumor burden was monitored weekly by bioluminescent imaging. All the mice were then humanely sacrificed under anesthesia on day 26.

2.5. The Tp53-deficient ID8 tumor-bearing C57BL/6 mouse model

5×10^6 *Tp53*-deficient ID8 cells were injected intraperitoneally into C57BL/6 mice. After 3 days of injection, mice were randomly assigned to the control group (n = 6), the niraparib (Beigene, 50 mg/kg, intragastrically) single agent group (n = 6), the Lipro-1 (MCE, 10 mg/kg, HY-12726, intraperitoneally) single agent group (n = 6), the SSO (MCE, 50 mg/kg, HY-112847A, intragastrically) single agent group (n = 6), the combined treatment of niraparib with Lipro-1 group (n = 6), the combined treatment of niraparib with SSO group (n = 6). Tumor burden was monitored by bioluminescent imaging, the number of abdominal lesions, and the volume of ascites at the endpoint. All the mice were then humanely sacrificed under anesthesia on day 26.

2.6. Cell culture

Human OC cell lines OVCAR8, SKOV3, and mouse OC cell line ID8 were purchased from the MD Anderson Cancer Center characterized Cell line Core. Human OC cell lines A2780 and OV90 were obtained from the American-type culture collection (ATCC, Rockville, MD, USA). A2780, OVCAR8, and ID8 were cultured in RPMI-1640 or DMEM medium supplemented with 1 % penicillin-streptomycin (Sigma, P4333) and 10 % fetal bovine serum (Gibco, A5669701). OV90 and SKOV3 were cultured in MCDB105/M199 or McCoy's 5A medium supplemented with 1 % penicillin-streptomycin and 10 % fetal bovine serum. OVCAR8 is a cell line with *BRCA1* methylation, whereas A2780, OV90, SKOV3, and ID8 are *BRCA*-wild type cell lines. In addition, OVCAR8 and OV90 are *TP53*-mutated cell lines, whereas A2780, SKOV3, and ID8 are *TP53* wild-type cell lines.

2.7. Cell transfection

CD36 small-interfering RNAs (siRNAs), *TP53* siRNAs, *FASN* siRNAs, *NFE2L2* siRNAs, control siRNAs, vector-overexpressing plasmids, and *TP53*-overexpressing plasmids were purchased from RiboBio Co. Ltd. (Guangzhou, China). The transfection of siRNA was performed using lipo3000 (Invitrogen, L3000075) according to the manufacturer's instructions, and the transfection of plasmid was performed using X-tremeGENE™ 9 DNA Transfection Reagent (Roche, 6365779001) according to the manufacturer's instructions. The knockdown or overexpression efficacy was assessed by real-time (RT) PCR after 48 h of transfection and by western blotting after 72 h of transfection. The siRNA sequences used were as follows (5′–3′)

Si-*CD36* 1, GCA GCAACATTCAAGTTAA.
Si-*CD36* 2, GGAATATATTGTGCCTAT.
Si-*CD36* 3, GCATGCAGATCGAAAACAA.
Si-*TP53* 1, GAAAUUUGCGUGUGGAGUATT.
Si-*TP53* 2, GCGCACAGAGGAAGAGAAUTT.
Si-*TP53* 3, ACCACUGGAUGGAGAAUAUTT.
Si-*FASN* 1, GCUGGAAGUCACCUAUGAAGCTT.
Si-*FASN* 2, CCGAGACACUCGUGGGCUACATT.
Si-*FASN* 3, GGCUCUCCUUCUUCUUCGACUTT.
Si-*NFE2L2* 1, CAUUGAUGUUUCUGAUCUAUCTT.
Si-*NFE2L2* 2, GCAGUUCAAUGAAGCUCAACUTT.
Si-*NFE2L2* 3, GACAGAAGUUGACAAUUAUCATT.

2.8. Cell viability assays

Tumor cells were seeded at 8×10^3 cells per well in 96-well plates and treated for 72 h with niraparib (Selleck, MK-4827, 10 μM), Ferr-1 (ferrostatin-1, MCE, HY-100579, 10 μM), SSO (MCE, HY-112847A, 100 μM), AA (arachidonic acid, MCE, HY-109590, 50 μM), OA (oleic

acid, MCE, HY-N1446, 50 μM), EPA (eicosapentaenoic acid, MCE, HY-B0660, 50 μM), PA (palmitic acid, MCE, HY-N0830, 50 μM), and MA (myristic acid, MCE, HY-N2041, 50 μM). The culture medium was then replaced with fresh medium containing 10 % Cell Counting Kit-8 (Vazyme, CCK8, China) reagent. Cell viability was measured according to the protocols.

2.9. Western blotting

Cell extracts were prepared in RIPA lysis buffer (Sigma, V900854) supplemented with protease inhibitor (Sigma, P8340). Protein for each sample was separated on sodium dodecyl sulfate-polyacrylamide gel electrophoresis gels and then transferred to the PVDF membrane. The membranes were incubated with skimmed milk (Sigma,115363) for 1 h at room temperature and then with anti-CD36 (Abcam, ab133625, 1:1000), anti-GAPDH (ABclonal, A19056, 1:1000), anti-FASN (CST, 3180, 1:1000), and anti-Vinculin (Abcam, ab129002, 1:1000) antibodies at 4 °C overnight. The membranes were then incubated with the appropriate HRP-linked secondary antibody (Abcam, ab6721, 1:5000) for 1 h at room temperature and were then visualized using an enhanced ECL system (Thermofisher, 32209).

2.10. Oil red O staining

For frozen sections, thaw the slides at room temperature overnight or for at least 1 h before staining. Then the frozen sections were stained using a Modified Oil Red O Staining Kit (Beyotime, C0158S) according to the protocols.

2.11. H&E staining

Tissues were stained with hematoxylin staining solution (Beyotime, C0107) and eosin staining solution (Beyotime, C0109) according to the protocols.

2.12. FerroOrange staining

Tumor cells were seeded in 24-well plates and treated with indicated drugs. Then, the cells were stained with 1 μM FerroOrange (Kumamoto, F374, Japan) for 30 min in the dark at 37 °C. The fluorescences of the cells were visualized under a fluorescence microscope.

2.13. Immunofluorescence (IF)

After being fixed in 4 % paraformaldehyde for 30 min, tumor cells were permeabilized with 0.4 % Triton X-100 for 20 min. Then, these fixed cells were blocked within 5 % BSA for 1 h at room temperature and incubated with an anti-NRF2 antibody (CST, 12721T, 1:100) overnight at 4 °C. After three washes with Tris Buffered Saline with Tween-20, Cells were incubated with FITC-conjugated secondary antibodies (CST, 4412, 1:200) for 1 h at room temperature, and the nuclear was stained with DAPI (Abcam, ab104139). Lastly, cells were visualized under a Confocal Laser Scanning Microscope (Leica).

2.14. IHC staining

The biopsy or surgically resected tumor samples were first paraffin-embedded and cut into slides. The slides were deparaffinized, hydrated, antigen retrieved, and incubated with the primary antibodies against CD36 (Abcam, ab133625, 1:100), 4-HNE (Abcam, ab46545, 1:100), and FASN (CST, 3180, 1:1000) overnight at 4 °C for IHC staining and incubated with horseradish peroxidase (HRP)-conjugated secondary antibody (Abcam, ab6721, 1:5000) for 1 h and then stained with the DAB Kit (Thermofisher, 34002). Slides were dehydrated, paraffinized embedded, and counterstained with hematoxylin (CST, 14166S).

2.15. Quantitative RT PCR

Total RNA was isolated using an RNA Extraction Kit (Vazyme, RC112-01) according to the manufacturer's standard protocols. For RT-PCR analysis, complementary DNA was synthesized using a cDNA Synthesis Kit (Vazyme, R423-01). RT-PCR was performed in triplicate (n = 3) on the Bio-Rad CFX96 system using the protocol provided by Vazyme. The threshold cycle (Ct) values of the target genes were normalized to those of *GAPDH*.

2.16. Primers

Gene	Primers
GAPDH	Fwd: AGATCCCTCCAAAATCAAGTGG
	Rev: GGCAGAGATGATGACCCTTTT
CD36	Fwd: CAGGTCAACCTATTGGTCAAGCC
	Rev: GCCTTCTCATCACCAATGGTCC
FASN	Fwd: TTCTACGGCTCCACGCTCTTCC
	Rev: GAAGAGTCTTCGTCAGCCAGGA
FABP4	Fwd: ACGAGAGGATGATAAACTGGTGG
	Rev: GCGAACTTCAGTCCAGGTCAAC
FABP3	Fwd: GTGGAGTTCGATGAGACAACAGC
	Rev: TGGTCTCTTGCCCGTCCCATTT
SLC27A1	Fwd: TGACAGTCGTCCTCCGCAAGAA
	Rev: CTTCAGCAGGTAGCGGCAGATC
SLC27A2	Fwd: GTGGAGAAAGATGAACCTGTCCG
	Rev: CTGAGCCTTTGCTCCAGCATAG
SLC27A3	Fwd: TGTGGTGTCCACCAGGAAGATG
	Rev: AACTGACCAGCCGAGAACTTGG
SCD	Fwd: CCTGGTTTCACTTGGAGCTGTG
	Rev: TGTGGTGAAGTTGATGTGCCAGC
CPT1A	Fwd: GATCCTGGACAATACCTCGGAG
	Rev: CTCCACAGCATCAAGAGACTGC
LPL	Fwd: CTGCTGGCATTGCAGGAAGTCT
	Rev: CATCAGGAGAAAGACGACTCGG
CPT2	Fwd: GCAGATGATGGTTGAGTGCTCC
	Rev: AGATGCCGCAGAGCAAACAAGTG
ACO1	Fwd: TCCTCAGGTGATTGGCTACAGG
	Rev: TCGGTCAGCAATGGACAACTGG
TP53	Fwd: CCTCAGCATCTTATCCGAGTGG
	Rev: TGGATGGTGGTACAGTCAGAGC
ALOX15	Fwd: TCAGGTTCCCTTGTTACCGC
	Rev: CAGCTCTTCTTCCCGGTGTT
NFE2L2	Fwd: AGGTTGCCCACATTCCCAAA
	Rev: AGTGACTGAAACGTAGCCGA

2.17. Lipid peroxidation and cytosolic ROS measurement

Experiments were performed according to the manufacturer's protocol. Briefly, cells were incubated in a humidified chamber at 37 °C with 5 % CO_2 for 30 min with a lipid peroxidation sensor (Thermofisher, D3861, 10 μM) or CM-H2DCFDA (Thermofisher, C6827, 10 μM) in cell culture medium. After incubation, cells were harvested and analyzed by flow cytometry within 2 h of staining. Results were then acquired using BD aka Fortessa X30 systems. Data were analyzed using FlowJo_V10 software (TreeStar).

2.18. BODIPY 500/510C12

Cells were incubated with 20 μM BODIPY 500/510C12 (Thermofisher, D3823) at 37 °C for 2–5 min and washed with PBS. Images were visualized by a fluorescence microscope.

2.19. Malondialdehyde (MDA) assay

Tumor tissues were homogenized and then quantified according to the protein content. Cellular MDA levels were measured using an MDA assay kit (Solarbio, BC0025).

2.20. Widely targeted metabolomic

As for hydrophilic compounds, the thawed sample was homogenized by a grinder (30 Hz). A 400 μL solution (Methanol: Water = 7:3, v/v) containing internal standard was added into 20 mg of the homogenized sample, and the mixture was shaken. After placing it on ice, the sample was centrifuged. A 200 μL aliquot of the supernatant was transferred for LC-MS analysis. As for hydrophobic compounds, 1 mL of the extraction solvent (MTBE: MeOH = 3: 1, v/v) containing internal standard mixture was added into the thawed sample. After whirling the mixture and water was added. Vortex and centrifuge, the upper organic layer was collected and evaporated using a vacuum concentrator. The dry extract was dissolved in 200 μL reconstituted solution (ACN: IPA = 1:1, v/v) to LC-MS/MS analysis.

After the acquirement of the raw data, the missing values were filled with 1/5 of the minimum value of each metabolite. Then, we calculated the CV (coefficient of variation) values for the QC samples and retained the metabolites with CV values less than 0.3 to obtain the final data file. We used the DESeq2 package (version 1.42.1) package to analyze the differentially enriched lipids between pre- and post-treatment metastatic lesions.

2.21. Bulk RNA sequencing (RNAseq)

RNA from 5 paired niraparib pre- or post-treated tumors in the metastatic lesions derived from the NANT clinical trial (Table 2) was extracted using the Rneasy Mini Kit (QIAGEN, 217084). Samples were sequenced on the Illumine Hiseq 4000 sequencer with 150 bp paired-end reads. The quality inspection results of all samples were qualified, and the total amount, purity, and integrity of the samples had achieved the requirements for library construction.

2.22. Gene set enrichment analysis (GSEA)

We used the DESeq2 package (version 1.42.1) package to analyze the differentially expressed genes related to lipid metabolism between the paired metastatic foci. The GSEA was performed using the clusterProfiler R (version 4.8.3) package.

2.23. Statistical analysis

All the results were analyzed using GraphPad Prism 6.0 and were presented as mean ± sd. Based on at least three independent experiments. Statistical significance between the two groups was calculated using the Student *t*-test. Comparisons between multiple groups were determined by a one-way analysis of variance followed by Tukey's post hoc test. $P < 0.05$ was considered statistically significant (*), $P < 0.01$ was considered highly significant (**), and $P < 0.001$ was considered extremely significant (***).

2.24. Data availability

The data from bulk RNAseq of paired tumor tissues from patients in the NANT clinical trial is available in OMIX (https://ngdc.cncb.ac.cn/omix/preview/ZAxvMET5) with accession number OMIX005792. Graphs of quantitative data and representative images of blot and gel generated in this study are available from the corresponding author upon reasonable request.

3. Results

3.1. Fatty-acid enriched ovarian cancer metastases are sensitive to niraparib treatment

To evaluate the responsiveness of OC disseminated lesions to niraparib treatment, we compared the paired pre- and post-treated tumor burden of patients enrolled in the NANT clinical trial based on peritoneal CT images [20]. We found that niraparib exposure significantly limited the progression of peritoneal metastatic lesions (Fig. 1A and B), indicating the susceptibility of OC metastases to this therapeutic intervention. Intraperitoneally disseminated lesions are well-known to be surrounded by adipose tissues [21]. To elucidate the association between the metastasis suppression by niraparib and abundant fatty acids, we sought to confirm whether the intratumoral environment of metastases was also rich in fatty acids. To this end, we performed the H&E and oil red O staining on clinical tumor samples of metastatic lesions. As expected, an abundance of lipid droplets was observed to disperse throughout the metastatic foci (Fig. 1C).

To further explore the contribution of fatty acids to the anti-tumor effects of niraparib, we cultured patient adipose tissues located at the omentum using 1640 medium containing charcoal-stripped FBS (fatty acid-free medium). After 48 h of culturing, the supernatant was collected as the patient-derived fatty acid medium. Then we mixed the fatty acid-free medium and patient-derived fatty acid medium at ratios of 1:0, 15:1, 7: 1, 3:1, 1:1, and 0:1 to culture OC cell lines, including OVCAR8 (*BRCA1* methylation), OV90 (*BRCA1* wildtype, *BRCA1* WT), A2780 (*BRCA1* WT), and SKOV3 (*BRCA1* WT) cells, under the treatment of niraparib. The results showed that patient-derived fatty acids significantly improved the sensitivity of both *BRCA* WT and dysfunctional OC cells to niraparib treatment (Fig. 1D). Consistently, the addition of exogenous fatty acids in culturing medium also facilitated the tumor-suppressive potential of niraparib on these cells (Fig. 1E). Given that the patient-derived fatty acids and commercial fatty acids were both mixtures, we next sought to determine which fatty acid contributed mostly to the enhanced tumor-inhibiting potential of niraparib. Five major components of fatty acids, including AA (arachidonic acid), OA (oleic acid), EPA (eicosapentaenoic acid), PA (palmitic acid), and MA (myristic acid), were employed to culture two OC cell types OVCAR8 and A2780 in the treatment of niraparib. Interestingly, among the five fatty acids, AA significantly enhanced the therapeutic efficacy of niraparib in both cell lines (Fig. 1F). Moreover, we performed widely targeted metabolomics on 19 niraparib pre-treated and 18 post-treated clinical frozen metastatic tissues to confirm our observation. Among the differentially expressed metabolites, Lipoxin B4 (LXB4), a metabolite of AA, was found to be most significantly upregulated under niraparib treatment (Fig. 1G). Previous studies have identified 15-LOX-1, encoded by the arachidonate 15-lipoxygenase (*ALOX15*) gene, as the enzyme responsible for converting AA to LXB4 [22]. Consistently, an enhanced mRNA level of *ALOX15* was observed following niraparib treatment, and the pivotal role of AA in the improved efficacy of niraparib was further confirmed (Fig. S1A). Taken together, these findings suggest that the preferential elimination of OC metastases by niraparib is closely associated with the rich fatty acids within tumor beds.

3.2. Niraparib enhances the uptake of fatty acids, leading to lipid peroxidation and subsequent ferroptosis in tumor cells

To decode the action of fatty acid in the facilitation of tumor suppressive capacity of niraparib on OC metastases, we conducted bulk RNAseq on OC metastases before and after niraparib monotherapy. GSEA revealed that niraparib played an important role in the reprogramming of lipid metabolism across lipid uptake and oxidation, as evidenced by significant upregulation of genes enriched in lipid localization, lipid storage, lipid droplet, lipid oxidation, lipid homeostasis, and lipid metabolism following treatment (Fig. 2A). To confirm the role of niraparib in the enhanced uptake of fatty acids by tumor cells, we cultured OVCAR8 and A2780 cells in a fatty acid-free medium. Then we added exogenous fatty acids into the medium and performed C1-BODIPY 500/510C12 staining. A significantly increased number of lipid droplets was reserved in the niraparib-treated cells (Figs. S2A–B). This phenomenon was also observed in OV90 and SKOV3 cells (Figs. S2C–D). To further verify these findings *in vivo*, we established a

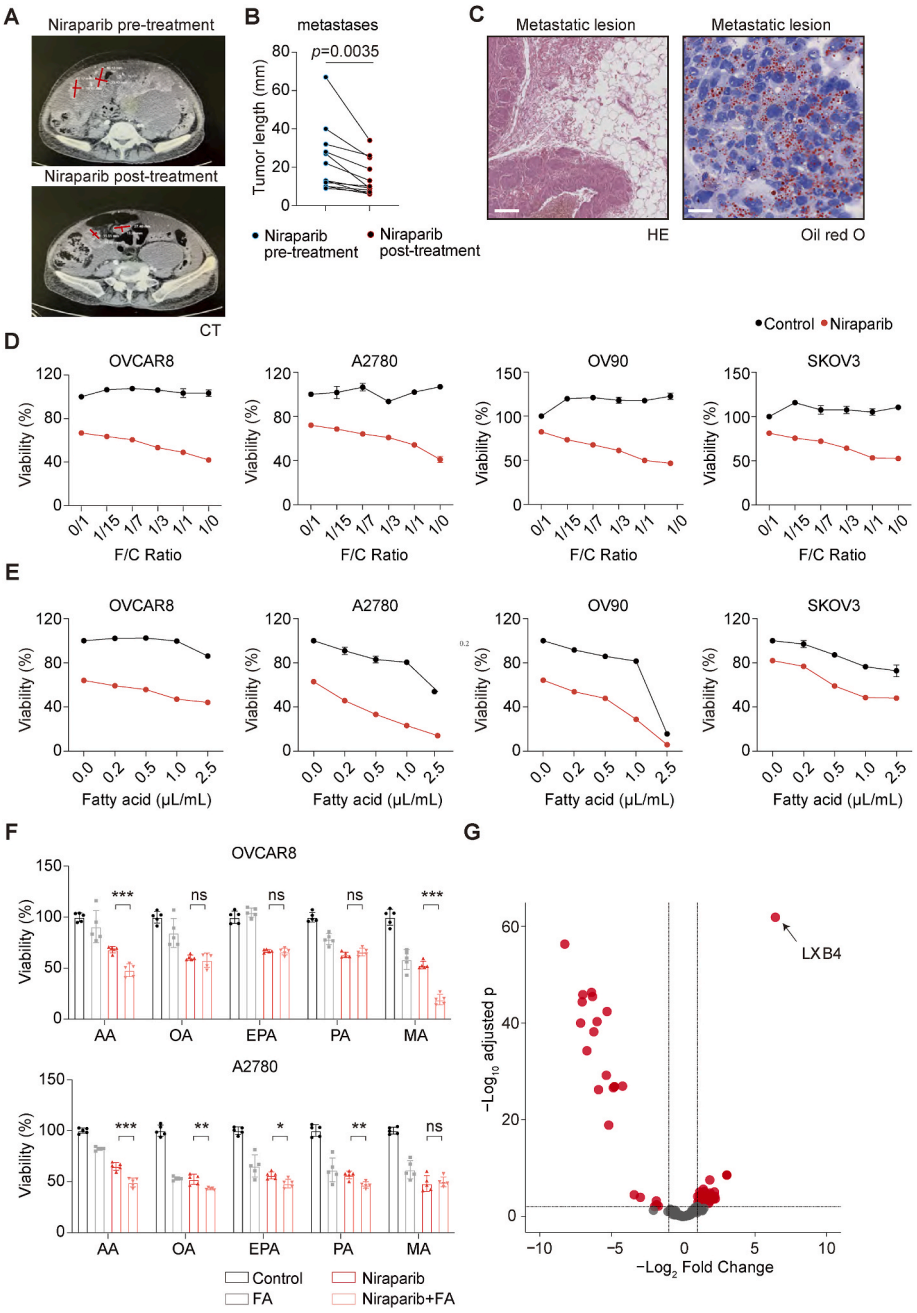

Fig. 1. Metastases enriched in fatty acids are sensitive to niraparib treatment. A, The representative cross-section on the computed tomography (CT) image of metastatic tumor tissue prior to niraparib treatment (upper) and after niraparib treatment (lower) from the patients enrolled in the NANT clinical trial. **B**, The CT images were obtained from patients (n = 13). The length of the cross-section was measured, and the *P* value was assessed by paired *t*-test. **C**, Representative hematoxylin and eosin (H&E) staining of tumors (left, scale bar = 100 μm) and oil red O staining (right, scale bar = 25 μm) in ovarian cancer (OC) metastatic sections from patients enrolled in the NANT clinical trial. **D**, OVCAR8, A2780, OV90, and SKOV3 cells were cultured in media mixing the fatty acid-free medium and the patient-derived fatty acid medium at various ratios (F/C Ratio) with the treatment of 10 μM niraparib for 72 h, and the cell viability was determined. **E**, OVCAR8, A2780, OV90, and SKOV3 cells were cultured in fatty acid-free media supplemented with 0, 0.2, 0.5, 1.0, and 2.5 μL/mL exogenous fatty acids with the treatment of 10 μM niraparib for 72 h, and the cell viability was determined. **F**, OVCAR8 and A2780 cells were cultured in fatty acid-free media supplemented with 50 μM AA (arachidonic acid), 50 μM OA (oleic acid), 50 μM EPA (eicosapentaenoic acid), 50 μM PA (palmitic acid), and 50 μM MA (myristic acid) with the treatment of 10 μM niraparib for 72 h, and the cell viability was determined. *P* values were assessed by Student *t*-test. *, $P < 0.05$; **, $P < 0.01$; ***, $P < 0.001$. **G**, Volcano plot of differentially enriched lipids between widely targeted metabolomics on 19 niraparib pre-treated and 18 post-treated clinical frozen metastatic tissues.

syngeneic mouse model by engrafting mouse OC ID8 cells into C57BL/6 mice and a PDX using BALB/c nude mice. Following a 3-week treatment of niraparib, we found more lipid droplets in niraparib-challenged ID8 and OC PDX tumors compared to untreated using oil red O staining (Fig. 2B). Importantly, histochemical analysis of the paired clinical OC metastatic tissues from the NANT trial before and after niraparib treatment also revealed a significant increase of lipid droplets within the tumors challenged by niraparib (Fig. 2C).

Excessive fatty acids often result in heightened peroxidation, closely associated with ferroptosis [23–25]. To determine the redox level in tumors, we cultured OVCAR8, A2780, OV90, and SKOV3 cells in a fatty acid-free medium containing exogenous fatty acids with or without niraparib treatment. Staining with the lipid peroxidation probe and detecting with flow cytometry, we found an enhanced lipid peroxidation

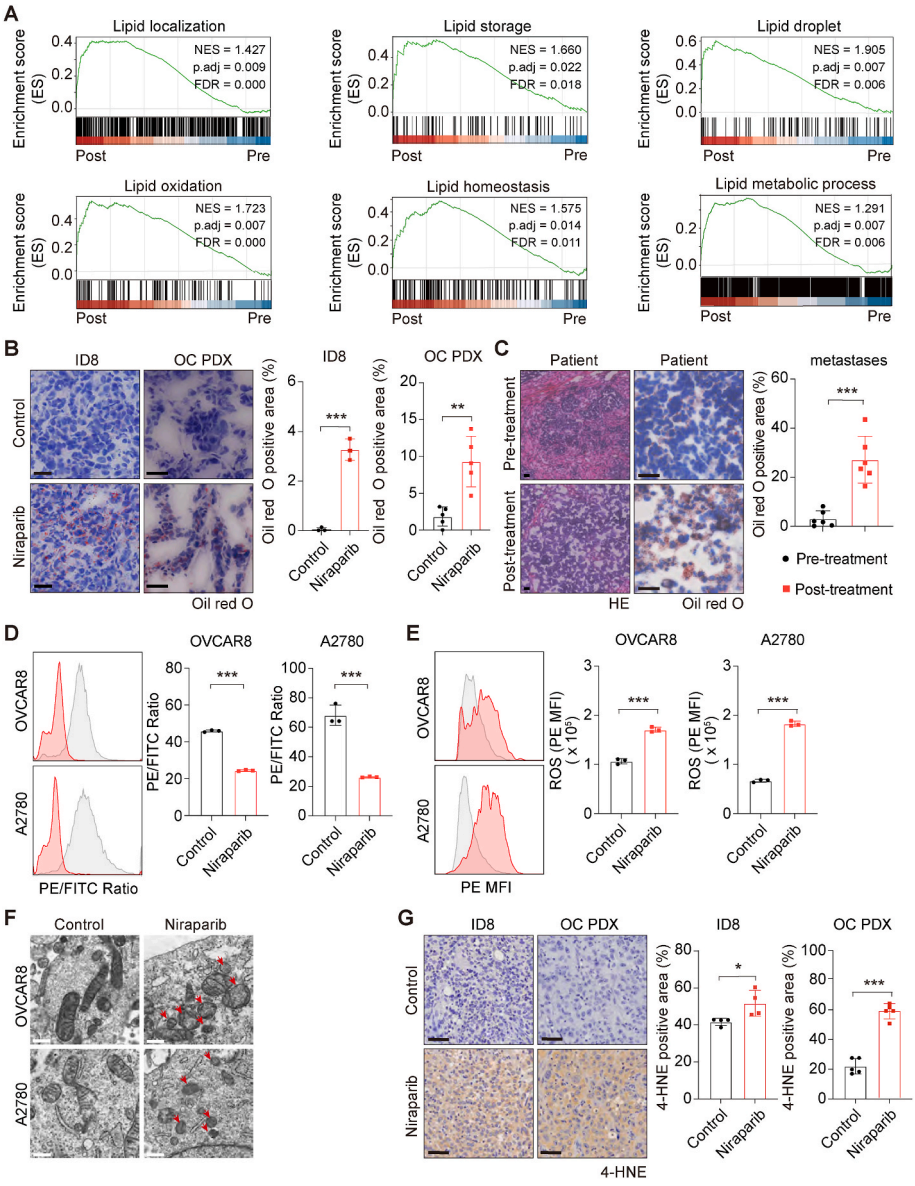

Fig. 2. Niraparib promotes fatty acid uptake and lipid peroxidation in tumor cells. A, Gene set enrichment analysis (GSEA) showed the changes of pathways related to lipid metabolism treated or untreated with niraparib in metastatic lesions. **B**, Representative images of oil red O staining in tissues derived from ID8 tumor-bearing mouse models (left, n = 3, scale bar = 50 μm) or human OC patient-derived xenograft (PDX) tissues (right, n = 5, scale bar = 100 μm) treated or untreated with niraparib. Oil red O positive staining proportion was measured by Image Pro Plus 6.0. **C**, Representative images of H&E staining (left, n = 6, scale bar = 50 μm) and oil red O staining (right, n = 6, scale bar = 50 μm) in paired clinical OC metastatic tissues from the NANT trial before and after niraparib treatment. Oil red O positive staining proportion was measured by Image Pro Plus 6.0. **D-E**, OVCAR8 and A2780 cells were cultured in fatty acid-free media in the presence of 1 μL/mL exogenous fatty acids and treated with 10 μM niraparib for 72 h. The lipid peroxidation level (**D**) and reactive oxygen species (ROS) level (**E**) were measured by flow cytometry. **F**, Representative transmission electron microscopy (TEM) images of mitochondrial morphology in the control group and the niraparib-treated group were presented. Red arrows indicate the mitochondrial atrophy (Scale bar = 500 nm). **G**, Representative images of immunohistochemistry (IHC) staining of 4-HNE in tissues derived from ID8 tumor-bearing mouse models (left, n = 4, Scale bar = 50 μm) or human OC PDX tissues (right, n = 5, Scale bar = 50 μm) treated or untreated with niraparib. 4-HNE positive staining proportion was measured by Image Pro Plus 6.0. **B-E**, and **G.** *P* values were assessed by Student *t*-test. *, $P < 0.05$; **, $P < 0.01$; ***, $P < 0.001$.

level within these niraparib-treated OC cells compared to the control (Fig. 2D–S2E). Accordingly, we witnessed an augmented reactive oxygen species (ROS) level in these cells after niraparib administration using ROS probe staining (Fig. 2E–S2F). To further validate the potential of niraparib to induce ferroptosis in a fatty acid-rich environment, we conducted transmission electron microscopy (TEM) and observed elevated mitochondria damage characterized by morphological alteration and the loss of cristae in niraparib-treated tumor cells (Fig. 2F). Also, FerroOrange staining showed increased Fe^{2+} concentration in the tumor cells upon niraparib treatment, providing consistent evidence supporting that niraparib triggered ferroptosis in a fatty acid-rich context (Figs. S2G–H). To verify this in tumor tissues, we conducted IHC staining for 4-HNE, a prominent biomarker for lipid peroxidation and ferroptosis, on ID8 and PDX tumors with or without exposure to niraparib. The results showed that niraparib administration significantly boosted the level of 4-HNE (Fig. 2G). Together, the above observations suggest that niraparib promotes the uptake of fatty acids and lipid peroxidation-induced ferroptosis, hinting at the possible mechanism by which niraparib could harness its anti-tumor effect against OC metastasis.

3.3. Niraparib triggers ferroptosis in a p53-independent manner by fatty acid uptake

To further characterize the ferroptosis induced by niraparib, a potent ferroptosis inhibitor ferrostatin-1 (Ferr-1) was used to pretreat OVCAR8 cells (*TP53* mutant, *TP53* Mut) and A2780 cells (*TP53* wild-type, *TP53* WT) in media with varying concentrations of fatty acids and niraparib exposure. Interestingly, we observed a differential response to Ferr-1 based on p53 status in the absence of fatty acids: Ferr-1 failed to reduce niraparib-induced lipid peroxidation and ROS levels in OVCAR8 cells (Fig. 3A and C, Fig. S3A), whereas it significantly suppressed these levels in A2780 cells (Fig. 3B and D, Fig. S3B). Moreover, Ferr-1 exerted its protective effect in OVCAR8 (Fig. 3E) and OV90 (Fig. S3C) cells harboring *TP53* mutations, whereas it significantly mitigated cell death induced by niraparib in A2780 (Fig. 3F) and SKOV3 (Fig. S3D) cells with WT *TP53*. This observation was consistent with published literature [26,27]. However, the p53-dependent manner was abolished in the context of fatty acid abundance: Ferr-1 effectively limited lipid peroxidation levels and tumor suppression of niraparib in both *TP53* WT and *TP53* Mut cells (Fig. 3A–F, Figs. S3A–D). To further substantiate this finding, we transfected OVCAR8 and OV90 with a *TP53*-overexpressing plasmid to restore its function (Figs. S3E–F). Subsequently, these engineered cells were exposed to niraparib and/or Ferr-1 in the presence of different concentrations of fatty acids. Ferr-1 successfully inhibited the anti-tumor capacity of niraparib on *TP53*-overexpressed OVCAR8 (Fig. 3G and H) and OV90 (Figs. S3I–J) cells in the absence of fatty acids. Importantly, in the presence of fatty acids, both OVCAR8 (Fig. 3G and H) and OV90 (Figs. S3I–J) cells with or without overexpression of *TP53* were sensitive to Ferr-1. Conversely, knocking down *TP53* in A2780 and SKOV3 using si-RNAs abrogated the reverse effect of Ferr-1 in the

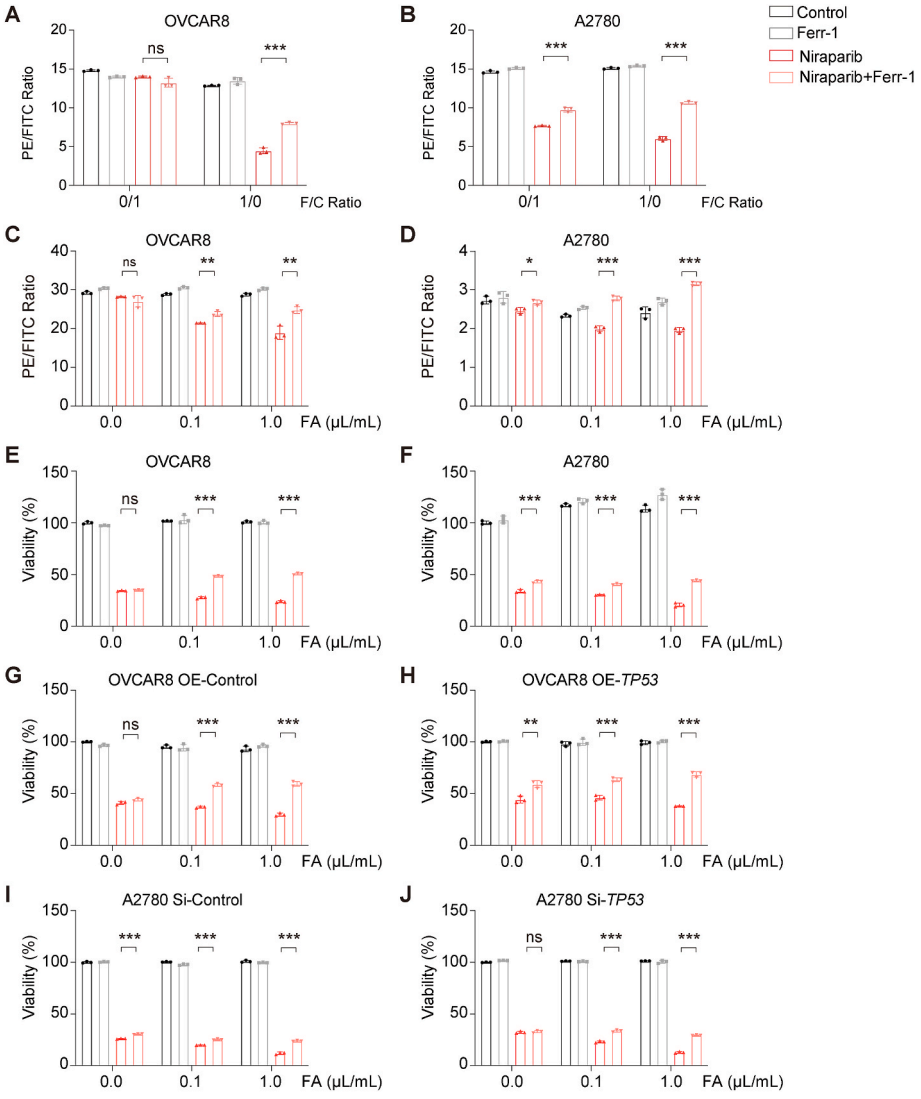

Fig. 3. The presence of fatty acids converts niraparib-induced ferroptosis to a p53-independent manner
A-B, OVCAR8 and A2780 cells were cultured in media mixing the fatty acid-free medium and the patient-derived fatty acid medium at various ratios with the treatment of 10 μM niraparib for 72 h. The lipid peroxidation levels were measured by flow cytometry. **C-D**, OVCAR8 and A2780 cells were cultured in fatty acid-free media supplemented with 0, 0.1, and 1.0 μL/mL exogenous fatty acids (FA) and treated with 10 μM niraparib, 10 μM Ferr-1 (ferrostatin-1), or a combination for 72 h. The lipid peroxidation levels were measured by flow cytometry. **E-F**, OVCAR8 and A2780 cells were cultured in fatty acid-free media supplemented with 0, 0.1, and 1.0 μL/mL exogenous FA and treated with 10 μM niraparib, 10 μM Ferr-1, or a combination for 72 h to assess cell viability. **G-H**, OVCAR8 cells were transfected with plasmids overexpressing vector (**G**) or *TP53* (**H**) and treated with 10 μM niraparib, 10 μM Ferr-1, or a combination in fatty acid-free media supplemented with 0, 0.1, and 1.0 μL/mL exogenous FA for 72 h to assess cell viability. **I-J**, A2780 cells were transfected with control siRNA (**I**) or *TP53*-siRNA (**J**) and treated with 10 μM niraparib, 10 μM Ferr-1, or a combination in fatty acid-free media supplemented with 0, 0.1, and 1.0 μL/mL exogenous FA for 72 h to assess cell viability. **A-J**, *P* values were assessed by Student *t*-test. ns, $P > 0.05$,*, $P < 0.05$; **, $P < 0.01$; ***, $P < 0.001$.

condition of no exogenous fatty acid supplementation, whereas Ferr-1 consistently reduced the tumor suppression by niraparib both in engineered cells and their control with the addition of fatty acids (Fig. 3I–J, S3G-H, S3K-L). Collectively, these findings suggest that fatty acids potentiate the anti-tumor effect of niraparib by inducing ferroptosis in a p53-independent manner, offering a potential for the shrinkage of abdominal dissemination, less constrained by the tumor's p53 status.

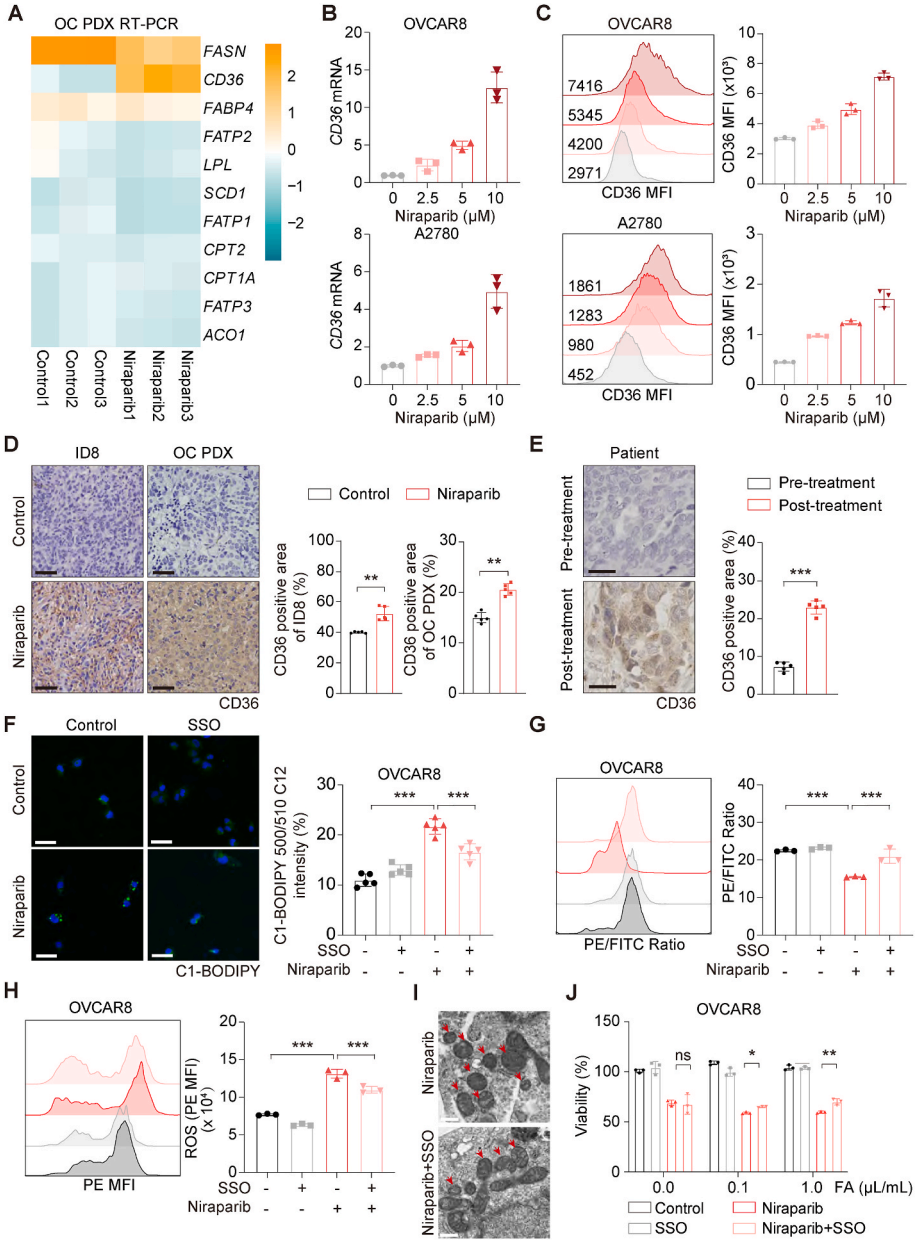

Fig. 4. CD36 is upregulated by niraparib, increasing fatty acid uptake and inducing ferroptosis. A, The mRNA levels of *FABP4*, *SCD*, *SLC27A1*, *CPT1A*, *CPT2*, *SLC27A2*, *ACO1*, *SLC27A3*, *LPL*, *FASN*, *CD36* were analyzed by RT-PCR in human OC tissues derived from PDX models treated or untreated with niraparib. **B**, *CD36* mRNA levels in OVCAR8 and A2780 cells were analyzed by RT-PCR after niraparib treatment for 48 h. **C**, After treatment with niraparib for 72 h, OVCAR8 and A2780 cells were stained with CD36 antibody and analyzed via flow cytometry. **D-E**, Representative images of IHC staining of CD36 in ID8 tumor tissues (left of **D**, n = 5, scale bar = 50 μm) or human OC tissues derived from PDX models with or without niraparib treatment (right of **D**, n = 5, scale bar = 50 μm) or derived from patients before and after niraparib treatment enrolled in the NANT clinical trial (**E**, n = 5, scale bar = 25 μm). CD36 positive staining proportion was measured by Image Pro Plus 6.0. **F**, OVCAR8 cells were cultured in fatty acid-free media supplemented with 1.0 μL/mL exogenous fatty acids and treated with 10 μM niraparib, 100 μM SSO (sulfosuccinimidyl oleate), or a combination for 72 h. Representative C1 BODIPY 500/510C12 staining images were shown. Scale bar = 50 μm. The intensity of C1 BODIPY 500/510C12 staining was assessed by Image Pro Plus 6.0. **G-H.** OVCAR8 cells were cultured in fatty acid-free media supplemented with 1.0 μL/mL exogenous fatty acids and treated with 10 μM niraparib, 100 μM SSO, or a combination for 72 h. The lipid peroxidation (**G**) and ROS (**H**) levels were measured by flow cytometry. **I.** Representative transmission electron microscopy (TEM) images of mitochondrial morphology in the niraparib-treated group and the combination of niraparib with the SSO group were presented. Red arrows indicate the mitochondrial atrophy (Scale bar = 500 nm). **J.** OVCAR8 cells were cultured in fatty acid-free media supplemented with 0, 0.1, 1.0 μL/mL exogenous fatty acids and treated with 10 μM niraparib, 100 μM SSO, or a combination for 72 h to assess cell viability. **D-E** and **J**, *P* values were assessed by Student *t*-test. **F–H**, *P* values were assessed by a one-way ANOVA test. ns, $P > 0.05$, *, $P < 0.05$; **, $P < 0.01$; ***, $P < 0.001$.

3.4. Niraparib induces ferroptosis by upregulating CD36 to enhance fatty acid uptake in OC cells

Next, we wondered about the underlying mechanism governing how niraparib enhanced fatty acid uptake. PDX tumors with or without niraparib treatment were subjected to determine the mRNA levels of the molecules related to fatty acid uptake and transport, including *FASN* [28], *FABP3*, *FABP4*, *SLC27A1*, *SLC27A2*, *SLC27A3*, *CD36* [29,30], *CPT1*, and *SCD* [31]. Interestingly, the gene expression of *FASN* was downregulated after treatment, yet it still maintained high levels of expression in tumors (Fig. 4A). However, the protein level of FASN was dramatically reduced by niraparib treatment, as evidenced by the analyses of western-blotting and IHC staining (Figs. S4A–C). As expected, the interference of *FASN* in OC cells exhibited no impact on cell viability after niraparib treatment (Figs. S4D–E). Of note, *CD36*, encoding the fatty acid transport receptor, was the most upregulated gene among tested members after niraparib challenge (Fig. 4A). To verify the effect of niraparib on CD36 expression on tumor cells *in vitro*, we treated OVCAR8, A2780, OV90, and SKOV3 cells with niraparib and then examined its levels of mRNA and protein by RT-PCR and flow cytometry, respectively. CD36 was upregulated at both transcriptional (Fig. 4B–S5A) and translational (Fig. 4C–S5B) levels in a dose-dependent manner. Furthermore, the increased expression of CD36 was confirmed by the IHC staining in murine ID8 tumors, PDX tumors (Fig. 4D), and clinical tumor samples obtained from the NANT trial (Fig. 4E). To substantiate that the facilitated fatty acid uptake was due to increased CD36

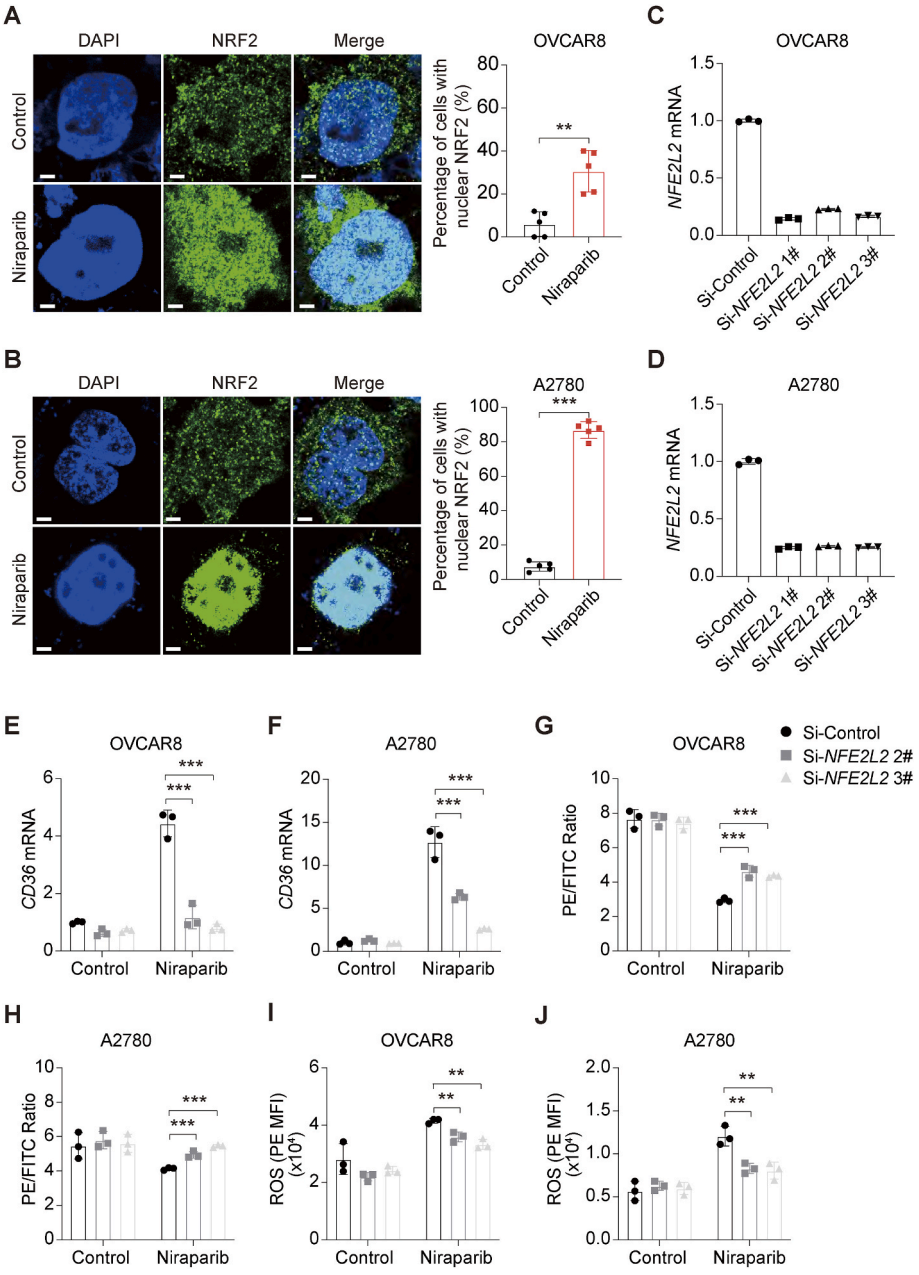

Fig. 5. NRF2 contributes to niraparib-induced CD36 upregulation. A-B, Representative IF images of DAPI (blue) and NRF2 (green) in OVCAR8 and A2780 cells after 10 μM niraparib treatment for 72 h (Scale bar = 3 μm). **C-D,** The knockdown efficiency of *NFE2L2*-siRNAs in OVCAR8 and A2780 cells was examined by RT-PCR. **E-F**, *CD36* mRNA levels in OVCAR8 and A2780 cells with depletion of *NFE2L2* were analyzed by RT-PCR after niraparib treatment for 48 h. **G-J**, After treatment with 10 μM niraparib in fatty acid-free media supplemented with 1.0 μL/mL exogenous fatty acids for 72 h, OVCAR8 and A2780 cells with depletion of *NFE2L2* were stained with lipid peroxidation probe and ROS probe. The lipid peroxidation (**G-H**) and ROS (**I-J**) levels were measured by flow cytometry. **A-B,** *P* values were assessed by Student *t*-test. **E-J**, *P* values were assessed by a one-way ANOVA test. *, $P < 0.05$; **, $P < 0.01$; ***, $P < 0.001$.

expression, a CD36 inhibitor sulfosuccinimidyl oleate (SSO) was employed in the determination of fatty acid uptake. The increased intracellular fatty acid levels by niraparib were significantly depleted upon SSO addition (Fig. 4F). Silencing *CD36* also inhibited fatty acid uptake under niraparib treatment in OVCAR8 cells (Figs. S5C–D). Accordingly, the niraparib-enhanced lipid peroxidation and ROS levels were attenuated by both SSO (Fig. 4G and H) and Si-*CD36* (Figs. S5E–F). Interference of *CD36* could also reduce the ferroptotic mitochondrials and promote the survival of niraparib-challenged OVCAR8 cells (Fig. 4I–J, S5G). Therefore, these data demonstrate that CD36 plays a pivotal role in mediating niraparib-induced fatty acid uptake and tumor cell ferroptosis.

3.5. NRF2 mediates niraparib-induced CD36 enhancement

It is well-established that the expression of CD36 is controlled by nuclear factor erythroid 2-related factor 2 (NRF2), which can be activated in response to DNA double-strand breaks [32,33]. Once activated, NRF2 acquires its transcriptional activity upon nuclear translocation [34]. Therefore, to explore whether the niraparib-induced upregulation of CD36 was due to NRF2 activation, we initially sought to verify an enhancement of NRF2 activity in response to niraparib treatment using IF assays. The results revealed that niraparib significantly facilitated the nuclear translocation of NRF2 (Fig. 5A and B). Then, we utilized siRNAs to knock down *NFE2L2* (gene for NRF2) expression, in order to determine its role in the upregulation of CD36 in the presence of niraparib (Fig. 5C and D). Undoubtedly, the effect of niraparib on CD36 expression was significantly abrogated when *NFE2L2* was interrupted (Fig. 5E and

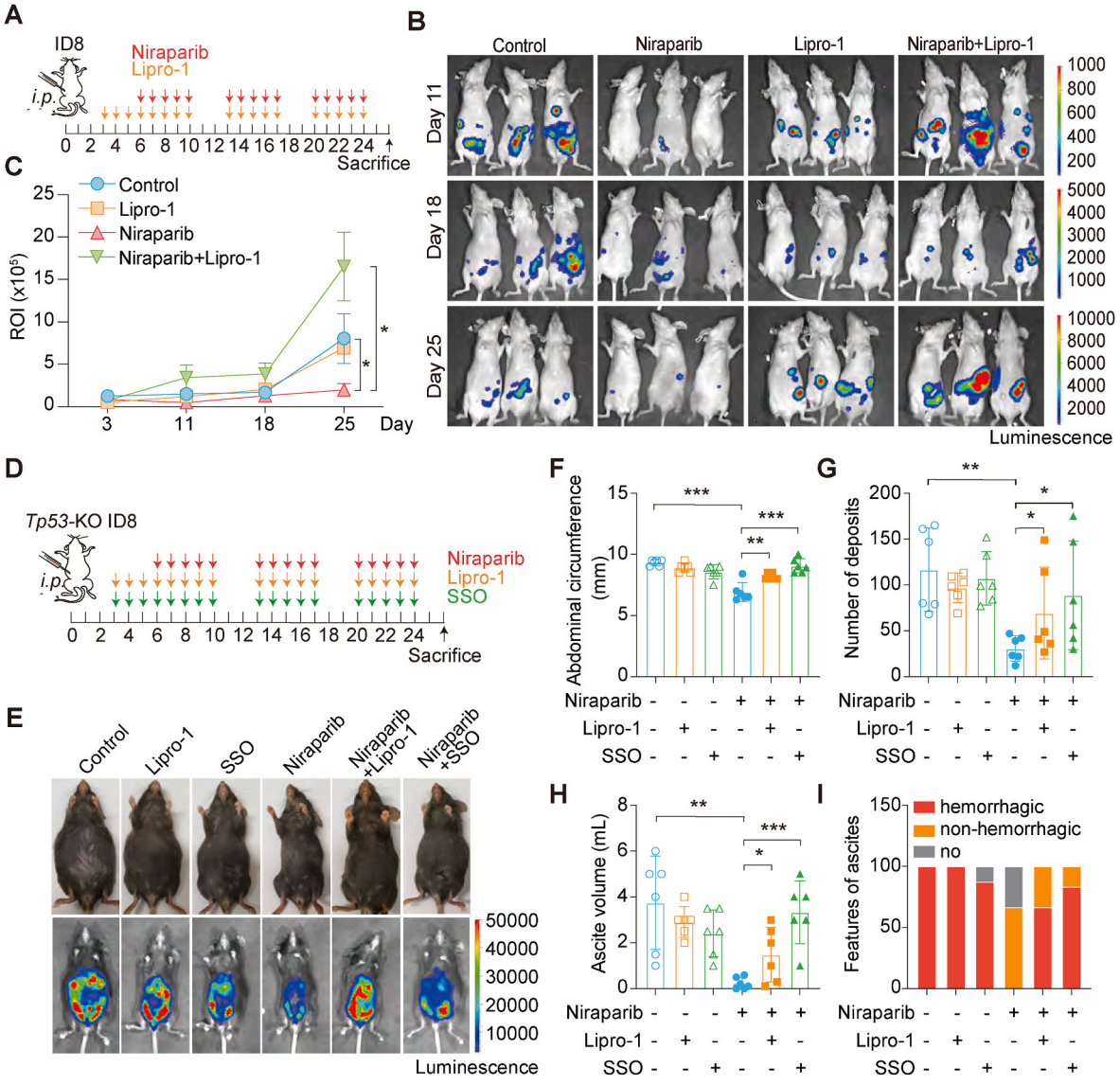

Fig. 6. Niraparib suppresses ovarian cancer via inducing ferroptosis *in vivo*. **A**, The schematic illustration of ID8 tumor-bearing model with BALB/c nude mice. Tumor-bearing mice were administered with niraparib (50 mg/kg) from day 6 and administered with Lipro-1 (liproxstatin-1, 10 mg/kg) from day 3. **B–C**, The bioluminescent images of each group every week after administration. The tumor burden was visualized by the intensity of bioluminescent imaging. **D**, The schematic illustration of *Tp53*-deficient ID8 tumor-bearing model with C57BL/6 mice. Tumor-bearing mice were administered with niraparib (50 mg/kg) from day 6, and administered with Lipro-1 (10 mg/kg) and SSO (sulfosuccinimidyl oleate, 50 mg/kg) from day 3. **E**, Representative actual or bioluminescent images of mice after a 3-week treatment. **F–H**, The length of the abdominal circumference (**F**), the number of abdominal lesions (**G**), and the volume of ascite (**H**) were quantified in each mouse treated with niraparib, with or without Lipro-1/SSO (n = 6). **I**, The feature of ascites was depicted in each mouse treated with niraparib, with or without Lipro-1/SSO (n = 6). **C**, *P* values were assessed by a two-way ANOVA test. **F–H**, *P* values were assessed by a one-way ANOVA test. *, $P < 0.05$; **, $P < 0.01$; ***, $P < 0.001$.

F). Consistently, the enhanced lipid peroxidation and ROS levels were also decreased in *NFE2L2*-silenced tumor cells compared to control cells (Fig. 5G–J). Taken together, these results suggest that NRF2 is critical for the upregulation of CD36 expression induced by niraparib.

3.6. Blocking ferroptosis and fatty acid uptake impair the tumor-suppressive ability of niraparib in vivo

As demonstrated above, niraparib initiated tumor cell ferroptosis dependent on augmented fatty acid uptake via CD36. We next attempted to investigate the critical role of ferroptosis and fatty acid uptake in the anti-tumor capacity of niraparib *in vivo*. We established an OC metastasis model by intraperitoneally injecting ID8 cells into immunodeficient BALB/c nude mice. These tumor-bearing mice were treated with niraparib alone or in combination with ferroptosis inhibitor liproxstatin-1 (Lipro-1) for 3 weeks (Fig. 6A). Dynamic bioluminescence images showed that niraparib effectively limited the tumor burden of intraperitoneal ID8, whereas Lipro-1 abolished this suppressive effect, verifying a benefit of niraparib in limiting metastatic lesions in a ferroptosis-dependent manner (Fig. 6B and C). This was further corroborated by the significant reduction in 4-HNE levels observed following treatment with Lipro-1 (Figs. S6A–B). In parallel, an OC PDX model was leveraged with niraparib and/or SSO challenge, and the tumor volume was monitored every other day (Figs. S6C–E). SSO significantly disturbed the sensitivity of tumors to niraparib (Figs. S6D–E) and diminished 4-HNE and MDA (malondialdehyde, another major product of lipid peroxidation) levels within tumors (Figs. S6F–H), confirming the pivotal role of CD36 in niraparib-triggered ferroptosis.

To further identify this in the immunocompetent mouse model, we generated *Tp53*-deficient ID8 cells by CRISPR/Cas9 [35] and transplanted intraperitoneally into female C57BL/6 mice. Following a 3-week exposure to niraparib, with or without Lipro-1 or SSO (Fig. 6D), the tumor burden was assessed by the measurement of bioluminescent intensity, the abdominal circumference, the number of abdominal lesions, and the ascite volume. The results suggested that both ferroptosis and CD36 inhibition significantly diminished the anti-tumor effect of niraparib in immunocompetent mice (Fig. 6E–H). In addition, the ascite of tumor-bearing mice was inclined to be hemorrhagic without treatment, whereas it disappeared or was non-hemorrhagic after niraparib treatment. However, the effect of niraparib on the features of ascites was abolished with the presence of Lipro-1 or SSO (Fig. 6I). Overall, our results further demonstrate that niraparib suppresses OC by inducing ferroptosis in a CD36-dependent manner in mouse models.

4. Discussion

In this study, employing CT images of clinical patients, we observed the ability of niraparib to effectively suppress OC metastases. This was because niraparib could induce ferroptosis on OC metastases by facilitating CD36 expression and fatty acid uptake, independent on the p53 status. The blockade of ferroptosis or CD36 function hindered the tumor-suppressive effect of PARPis *in vitro* and *in vivo*. Taken together, our findings provided a novel insight into niraparib's capacity in dissemination shrinkage, broadening the horizons of augmenting the anti-tumor effect of PARPis in OC.

Within the tumor microenvironment (TME), lipids actively contribute to metastasis, primarily by facilitating the tumor cell epithelial-to-mesenchymal transition (EMT) in concert with other TME components [36]. Consequently, interfering lipid metabolism and transport may augment the efficacy of anti-tumor therapy in metastasis [37,38]. Conversely, long-chain fatty acids upregulate major histocompatibility complex class I (MHC-I) expression on tumor cells to enhance the efficacy of immunotherapy, and lipid metabolites have been observed to enhance the anti-tumor activity of $CD8^+$ T cells [39,40]. Therefore, the dual role of lipids in both promoting and inhibiting tumor progression presents a complex and nuanced landscape in OC metastasis therapy. Here, based on the paired CT images and specimens derived from the NANT clinical trial, we show that the high lipid content in the metastasis enhances the anti-tumor capacity of niraparib. This observation advances the knowledge of lipid acids in improving the efficacy of cancer intervention.

Studies have shed light on the diverse cell deaths triggered by PARPis. They induce sustained DNA damage and replication stress, which in turn lead to tumor cell apoptosis [41–43]. PARPis have been shown to elicit the cleavage of gasdermins, initiating a form of programmed cell death known as pyroptosis [44–46]. In addition to these mechanisms, PARPis have brought to light their capacity to trigger OC cell ferroptosis in a p53-dependent manner through various mechanisms: the suppression of key enzymes such as glutathione peroxidase 4 (GPX4) [27], stearoyl-CoA desaturase 1 (SCD1) [47] or the solute carrier family 7 member 11 (SLC7A11) [26]. Consistently, niraparib has been observed to trigger ferroptosis in *TP53* WT OC cell lines in this study. In an intriguing twist, OC cell lines with *TP53* Mut undergo ferroptosis after niraparib exposure in the presence of fatty acids. This finding suggests that niraparib elicits ferroptosis in OC metastasis regardless of its p53 status, broadening its application in OC treatment given that the majority of OC patients harbor *TP53* mutation.

Ferroptosis, a mode of non-apoptotic cell death [48], is elicited by an iron-dependent accumulation of ROS and the subsequent lipid peroxidation [49–51]. A cohort of molecules pivotal in the realm of fatty acid metabolism and transport, including stearoyl-CoA desaturase-1 (SCD1), fatty acid binding protein-4 (FABP4), the long-chain fatty acid CoA ligase 4 (ASCL4), and CD36, either confer protection against or sensitize cells to ferroptotic cell death [29,52,53]. Specifically, CD36 facilitates lipid peroxidation by the uptake of oxidized lipids and polyunsaturated fatty acids, impairing the antitumor effects of $CD8^+$ T cells and $CD4^+$ T cells in a ferroptosis-dependent manner [54–57]. Palmitic acid has been reported to induce endoplasmic reticulum stress-dependent ferroptosis in colon cancer cells with high CD36 expression [58]. In our study, the major component of fatty acids, AA, was found to contribute to the enhancement of niraparib-induced ferroptosis in OC cells. Moreover, we observed that niraparib-induced tumor cell fatty acid accumulation and ferroptosis were mediated by the upregulation of CD36 in an NRF2-dependent manner. Taken together, our finding highlights the significance of CD36 in the suppression of OC metastases by niraparib.

Recently, based on the NANT clinical trial we initiated, niraparib has achieved a response rate of 62.5 % per RECIST (Response Evaluation Criteria in Solid Tumors) v.1.1 and 73.6 % per GCIG (Gynecologic cancer Intergroup) CA125 as neoadjuvant monotherapy [35]. In this study, we unveil that niraparib exhibits a proficient inhibition of metastatic lesions, thus bolstering the rationale for its application as a neoadjuvant therapeutic modality in advanced OC patients. Mechanistic exploration has established that niraparib induces tumor cell ferroptosis through the upregulation of CD36 expression and subsequent excessive uptake of fatty acid. These findings identify a hitherto unexplored mechanism in addition to the therapeutic prowess of niraparib, greatly advancing our understanding of the pharmacological impact of this drug.

CRediT authorship contribution statement

Ning Jin: Conceptualization, Data curation, Investigation, Methodology, Writing – original draft, Writing – review & editing. **Yi-yu Qian:** Data curation, Investigation, Methodology. **Xiao-fei Jiao:** Data curation, Formal analysis, Methodology. **Zhen Wang:** Investigation, Methodology. **Xin Li:** Investigation, Methodology. **Wen Pan:** Methodology, Software. **Jin-kai Jiang:** Methodology. **Pu Huang:** Investigation, Methodology. **Si-yuan Wang:** Investigation, Methodology. **Ping Jin:** Methodology. **Qing-lei Gao:** Funding acquisition, Supervision. **Dan Liu:** Funding acquisition, Supervision. **Yu Xia:** Conceptualization, Supervision, Writing – review & editing.

Authors' disclosures

No disclosures were reported.

Declaration of competing interest

All authors disclosed no relevant relationships.

Acknowledgments

This work was supported by the National Key Technology Research and Development Programme of China (2022YFC2704200), the Natural Science Foundation of Hubei Province (2023AFB760 and 2024AFB029), the National Science Foundation of China (82372928, 81802611 and 82403749).

Appendix A. Supplementary data

Supplementary data to this article can be found online at https://doi.org/10.1016/j.redox.2025.103528.

References

[1] U.A. Matulonis, A.K. Sood, L. Fallowfield, B.E. Howitt, J. Sehouli, B.Y. Karlan, Ovarian cancer, Nat. Rev. Dis. Prim. 2 (2016) 16061.
[2] R.L. Siegel, K.D. Miller, N.S. Wagle, A. Jemal, Cancer statistics, 2023, Ca - Cancer J. Clin. 73 (2023) 17–48.
[3] Z. Luo, Q. Wang, W.B. Lau, B. Lau, L. Xu, L. Zhao, et al., Tumor microenvironment: the culprit for ovarian cancer metastasis? Cancer Lett. 377 (2016) 174–182.
[4] Y. Wang, A.J. Duval, M. Adli, D. Matei, Biology-driven therapy advances in high-grade serous ovarian cancer, J. Clin. Investig. 134 (2024).
[5] S. Lheureux, M. Braunstein, A.M. Oza, Epithelial ovarian cancer: evolution of management in the era of precision medicine, Ca - Cancer J. Clin. 69 (2019) 280–304.
[6] D.K. Armstrong, R.D. Alvarez, F.J. Backes, J.N. Bakkum-Gamez, L. Barroilhet, K. Behbakht, et al., NCCN Guidelines® insights: ovarian cancer, version 3.2022, J. Natl. Compr. Cancer Netw. 20 (2022) 972–980.
[7] A. du Bois, T. Baert, I. Vergote, Role of neoadjuvant chemotherapy in advanced epithelial ovarian cancer, J. Clin. Oncol. 37 (2019) 2398–2405.
[8] J. Liu, X. Jiao, Q. Gao, Neoadjuvant chemotherapy-related platinum resistance in ovarian cancer, Drug Discov. Today 25 (2020) 1232–1238.
[9] J. Xu, Y. Fang, K. Chen, S. Li, S. Tang, Y. Ren, et al., Single-cell RNA sequencing reveals the tissue architecture in human high-grade serous ovarian cancer, Clin. Cancer Res. 28 (2022) 3590–3602.
[10] M. Raab, I. Kostova, S. Peña-Llopis, D. Fietz, M. Kressin, S.M. Aberoumandi, et al., Rescue of p53 functions by in vitro-transcribed mRNA impedes the growth of high-grade serous ovarian cancer, Cancer Commun (Lond) 44 (2024) 101–126.
[11] G.L. Scaglione, S. Pignata, A. Pettinato, C. Paolillo, D. Califano, G. Scandurra, et al., Homologous recombination deficiency (HRD) scoring, by means of two different shallow whole-genome sequencing pipelines (sWGS), in ovarian cancer patients: a comparison with myriad MyChoice assay, Int. J. Mol. Sci. 24 (2023).
[12] T. Qin, G. Chen, Recent advances in targeted therapy for ovarian cancer, Oncol. Transl. Med. 8 (2022).
[13] K.N. Moore, A.A. Secord, M.A. Geller, D.S. Miller, N. Cloven, G.F. Fleming, et al., Niraparib monotherapy for late-line treatment of ovarian cancer (QUADRA): a multicentre, open-label, single-arm, phase 2 trial, Lancet Oncol. 20 (2019) 636–648.
[14] M.R. Mirza, B.J. Monk, J. Herrstedt, A.M. Oza, S. Mahner, A. Redondo, et al., Niraparib maintenance therapy in platinum-sensitive, recurrent ovarian cancer, N. Engl. J. Med. 375 (2016) 2154–2164.
[15] X.H. Wu, J.Q. Zhu, R.T. Yin, J.X. Yang, J.H. Liu, J. Wang, et al., Niraparib maintenance therapy in patients with platinum-sensitive recurrent ovarian cancer using an individualized starting dose (NORA): a randomized, double-blind, placebo-controlled phase III trial, Ann. Oncol. 32 (2021) 512–521.
[16] N. Li, J. Zhu, R. Yin, J. Wang, L. Pan, B. Kong, et al., Treatment with niraparib maintenance therapy in patients with newly diagnosed advanced ovarian cancer: a phase 3 randomized clinical trial, JAMA Oncol. 9 (2023) 1230–1237.
[17] A. González-Martín, B. Pothuri, I. Vergote, R. DePont Christensen, W. Graybill, M. R. Mirza, et al., Niraparib in patients with newly diagnosed advanced ovarian cancer, N. Engl. J. Med. 381 (2019) 2391–2402.
[18] D.M. O'Malley, New therapies for ovarian cancer, J. Natl. Compr. Cancer Netw. 17 (2019) 619–621.
[19] V. Garg, A.M. Oza, Treatment of ovarian cancer beyond PARP inhibition: current and future options, Drugs 83 (2023) 1365–1385.
[20] D. Zhou, J. Liu, R. Liu, H. Li, Y. Huang, D. Ma, et al., Effectiveness and safety of niraparib as neoadjuvant therapy in advanced ovarian cancer with homologous recombination deficiency (NANT): study protocol for a prospective, multicenter, exploratory, phase 2, single-arm study, Front. Oncol. 12 (2022) 852772.
[21] M. Martin-Perez, U. Urdiroz-Urricelqui, C. Bigas, S.A. Benitah, The role of lipids in cancer progression and metastasis, Cell Metab. 34 (2022) 1675–1699.
[22] B. Wang, L. Wu, J. Chen, L. Dong, C. Chen, Z. Wen, et al., Metabolism pathways of arachidonic acids: mechanisms and potential therapeutic targets, Signal Transduct. Targeted Ther. 6 (2021) 94.
[23] M. Dodson, R. Castro-Portuguez, D.D. Zhang, NRF2 plays a critical role in mitigating lipid peroxidation and ferroptosis, Redox Biol. 23 (2019) 101107.
[24] F. Ursini, M. Maiorino, Lipid peroxidation and ferroptosis: the role of GSH and GPx4, Free Radic. Biol. Med. 152 (2020) 175–185.
[25] R.J. Wedan, J.Z. Longenecker, S.M. Nowinski, Mitochondrial fatty acid synthesis is an emergent central regulator of mammalian oxidative metabolism, Cell Metab. 36 (2024) 36–47.
[26] T. Hong, G. Lei, X. Chen, H. Li, X. Zhang, N. Wu, et al., PARP inhibition promotes ferroptosis via repressing SLC7A11 and synergizes with ferroptosis inducers in BRCA-proficient ovarian cancer, Redox Biol. 42 (2021) 101928.
[27] W. Yue, G. Yupeng, C. Jun, J. Kui, Apatinib combined with olaparib induces ferroptosis via a p53-dependent manner in ovarian cancer, J. Cancer Res. Clin. Oncol. 149 (2023) 8681–8689.
[28] A.J. Hoy, S.R. Nagarajan, L.M. Butler, Tumour fatty acid metabolism in the context of therapy resistance and obesity, Nat. Rev. Cancer 21 (2021) 753–766.
[29] Y. Chen, J. Zhang, W. Cui, R.L. Silverstein, CD36, a signaling receptor and fatty acid transporter that regulates immune cell metabolism and fate, J. Exp. Med. 219 (2022).
[30] R.E. Gimeno, Fatty acid transport proteins, Curr. Opin. Lipidol. 18 (2007) 271–276.
[31] R.J.A. Wanders, F.M. Vaz, H.R. Waterham, S. Ferdinandusse, Fatty acid oxidation in peroxisomes: enzymology, metabolic crosstalk with other organelles and peroxisomal disorders, Adv. Exp. Med. Biol. 1299 (2020) 55–70.
[32] X. Sun, Y. Wang, K. Ji, Y. Liu, Y. Kong, S. Nie, et al., NRF2 preserves genomic integrity by facilitating ATR activation and G2 cell cycle arrest, Nucleic Acids Res. 48 (2020) 9109–9123.
[33] T. Ishii, K. Itoh, E. Ruiz, D.S. Leake, H. Unoki, M. Yamamoto, et al., Role of Nrf2 in the regulation of CD36 and stress protein expression in murine macrophages: activation by oxidatively modified LDL and 4-hydroxynonenal, Circ. Res. 94 (2004) 609–616.
[34] C. Lisk, J. McCord, S. Bose, T. Sullivan, Z. Loomis, E. Nozik-Grayck, et al., Nrf2 activation: a potential strategy for the prevention of acute mountain sickness, Free Radic. Biol. Med. 63 (2013) 264–273.
[35] Y. Luo, Y. Xia, D. Liu, X. Li, H. Li, J. Liu, et al., Neoadjuvant PARPi or chemotherapy in ovarian cancer informs targeting effector Treg cells for homologous-recombination-deficient tumors, Cell 187 (18) (2024), 4905-4925. e24.
[36] S. Balaji, U. Kim, V. Muthukkaruppan, A. Vanniarajan, Emerging role of tumor microenvironment derived exosomes in therapeutic resistance and metastasis through epithelial-to-mesenchymal transition, Life Sci. 280 (2021) 119750.
[37] K.M. Nieman, H.A. Kenny, C.V. Penicka, A. Ladanyi, R. Buell-Gutbrod, M. R. Zillhardt, et al., Adipocytes promote ovarian cancer metastasis and provide energy for rapid tumor growth, Nat. Med. 17 (2011) 1498–1503.
[38] Y. Xuan, H. Wang, M.M. Yung, F. Chen, W.-S. Chan, Y.-S. Chan, et al., SCD1/FADS2 fatty acid desaturases equipoise lipid metabolic activity and redox-driven ferroptosis in ascites-derived ovarian cancer cells, Theranostics 12 (2022) 3534–3552.
[39] Y. Lai, Y. Gao, J. Lin, F. Liu, L. Yang, J. Zhou, et al., Dietary elaidic acid boosts tumoral antigen presentation and cancer immunity via ACSL5, Cell Metab. 36 (2024).
[40] Y. He, L. Fu, Y. Li, W. Wang, M. Gong, J. Zhang, et al., Gut microbial metabolites facilitate anticancer therapy efficacy by modulating cytotoxic CD8+ T cell immunity, Cell Metab. 33 (2021).
[41] C.J. Lord, A. Ashworth, PARP inhibitors: synthetic lethality in the clinic, Science 355 (2017) 1152–1158.
[42] J.A. Muñoz-Gámez, J.M. Rodríguez-Vargas, R. Quiles-Pérez, R. Aguilar-Quesada, D. Martín-Oliva, G. de Murcia, et al., PARP-1 is involved in autophagy induced by DNA damage, Autophagy 5 (2009) 61–74.
[43] M. Cahuzac, P. Langlois, B. Péant, H. Fleury, A.-M. Mes-Masson, F. Saad, Pre-activation of autophagy impacts response to olaparib in prostate cancer cells, Commun. Biol. 5 (2022) 251.
[44] C. Kim, X.-D. Wang, S. Jang, Y. Yu, PARP1 inhibitors induce pyroptosis via caspase 3-mediated gasdermin E cleavage, Biochem. Biophys. Res. Commun. 646 (2023) 78–85.
[45] S. Wang, C.-W. Chang, J. Huang, S. Zeng, X. Zhang, M.-C. Hung, et al., Gasdermin C sensitizes tumor cells to PARP inhibitor therapy in cancer models, J. Clin. Investig. 134 (2024).
[46] Y. Xia, P. Huang, Y.-Y. Qian, Z. Wang, N. Jin, X. Li, et al., PARP inhibitors enhance antitumor immune responses by triggering pyroptosis via TNF-caspase 8-GSDMD/E axis in ovarian cancer, J. Immunother. Cancer 12 (2024).
[47] S. Tang, Y. Shen, X. Wei, Z. Shen, W. Lu, J. Xu, Olaparib synergizes with arsenic trioxide by promoting apoptosis and ferroptosis in platinum-resistant ovarian cancer, Cell Death Dis. 13 (2022) 826.
[48] S.J. Dixon, Ferroptosis: bug or feature? Immunol. Rev. 277 (2017) 150–157.
[49] H. Yu, P. Guo, X. Xie, Y. Wang, G. Chen, Ferroptosis, a new form of cell death, and its relationships with tumourous diseases, J. Cell Mol. Med. 21 (2017) 648–657.
[50] Y. Qiu, Y. Cao, W. Cao, Y. Jia, N. Lu, The application of ferroptosis in diseases, Pharmacol. Res. 159 (2020) 104919.
[51] B. Hassannia, P. Vandenabeele, T. Vanden Berghe, Targeting ferroptosis to iron out cancer, Cancer Cell 35 (2019) 830–849.
[52] G. Luis, A. Godfroid, S. Nishiumi, J. Cimino, S. Blacher, E. Maquoi, et al., Tumor resistance to ferroptosis driven by Stearoyl-CoA Desaturase-1 (SCD1) in cancer

cells and Fatty Acid Biding Protein-4 (FABP4) in tumor microenvironment promote tumor recurrence, Redox Biol. 43 (2021) 102006.
[53] S. Doll, B. Proneth, Y.Y. Tyurina, E. Panzilius, S. Kobayashi, I. Ingold, et al., ACSL4 dictates ferroptosis sensitivity by shaping cellular lipid composition, Nat. Chem. Biol. 13 (2017) 91–98.
[54] S. Xu, O. Chaudhary, P. Rodríguez-Morales, X. Sun, D. Chen, R. Zappasodi, et al., Uptake of oxidized lipids by the scavenger receptor CD36 promotes lipid peroxidation and dysfunction in CD8 T cells in tumors, Immunity 54 (2021).
[55] X. Ma, L. Xiao, L. Liu, L. Ye, P. Su, E. Bi, et al., CD36-mediated ferroptosis dampens intratumoral CD8 T cell effector function and impairs their antitumor ability, Cell Metab. 33 (2021).
[56] CD36 activity causes ferroptosis in tumor-infiltrating CD8+ T cells, Cancer Discov. 11 (2021) OF24.
[57] Q. Xiao, L. Yan, J. Han, S. Yang, Y. Tang, Q. Li, et al., Metabolism-dependent ferroptosis promotes mitochondrial dysfunction and inflammation in CD4+ T lymphocytes in HIV-infected immune non-responders, EBioMedicine 86 (2022) 104382.
[58] H. Kuang, X. Sun, Y. Liu, M. Tang, Y. Wei, Y. Shi, et al., Palmitic acid-induced ferroptosis via CD36 activates ER stress to break calcium-iron balance in colon cancer cells, FEBS J. 290 (2023) 3664–3687.